Chapter 13
Investigation of the Unsteady Aerodynamics of Insect Flight: The Use of Immersed Boundary Method

Srinidhi Nagarada Gadde, Y. Sudhakar, and S. Vengadesan

13.1 Introduction

The current chapter summarizes the insect flight research carried out in the group of Prof. S. Vengadesan at IIT Madras, with immersed boundary methods (IBM) as the research tool. While most of the insects employ a symmetric wing motion along a horizontal stroke plane (e.g., fruit-flies, bees, and beetles), a few insects (e.g., dragonflies and hover-flies) translate their wings asymmetrically along a more inclined stroke plane. Our work focuses on the unsteady aerodynamics involved in the inclined stroke plane motions, and we address the following aspects of such a flight with numerical simulations of idealized two-dimensional kinematics of insect wings:

- Mechanism of vertical force generation
- Influence of multiple wings and their relative kinematics on force generation
- The effect of ground on vortex dynamics and force generation.

S. N. Gadde
Physics of Fluids Group, University of Twente, 7500 AE Enschede, The Netherlands
e-mail: s.nagaradagadde@utwente.nl

Y. Sudhakar
School of Mechanical Sciences, Indian Institute of Technology Goa,
Ponda, Goa 403401, India
e-mail: sudhakar@iitgoa.ac.in

S. Vengadesan (✉)
Department of Applied Mechanics, IIT Madras, Chennai 600036, India
e-mail: vengades@iitm.ac.in

S. Roy et al. (eds.), *Immersed Boundary Method*, Computational Methods
in Engineering & the Sciences, https://doi.org/10.1007/978-981-15-3940-4_13

13.1.1 Brief Review of Insect Aerodynamics

The study of insect flight is fascinating in its own right due to the underlying unsteady aerodynamics. Moreover, the knowledge gained from such studies will greatly benefit the designing of micro-aerial vehicles (MAVs) which has potential applications in military reconnaissance, weather monitoring, and information gathering. Here, we provide a very brief review of the unsteady aerodynamics involved in the insect flight. Extensive details can be found in the comprehensive reviews available in the literature (Sane 2003; Platzer et al. 2008; Shyy et al. 2010).

By using high-speed photography, Ellington (1984a) found that a typical flapping flight of an insect consists of two translational (upstroke and downstroke) and two rotational (pronation and supination) motions. To explain the aerodynamics involved in the aforementioned complex kinematics, classical potential flow aerodynamics and quasi-steady-state theories have been proposed. Quasi-steady-state theories assume that instantaneous forces on a flapping wing are equivalent to those for steady motion at the same instantaneous velocity and angle of attack. By comparing the theoretical results with experimental observations, Ellington (1984b) proved that conventional quasi-steady-state theories are insufficient to explain the enhanced lift force observed in the flight of hovering insects. The failure of such theories strongly suggests that unsteady aerodynamic mechanisms play a key role in the flapping flight. Previous experimental and numerical studies have uncovered three important unsteady mechanisms in flapping flight:

- Delayed stall: Stable attached leading-edge vortices (LEVs) are formed over the insect wings even when their angle of attack (AoA) is as high as 40° (Ellington et al. 1996). These attached LEVs greatly enhance the lift force on flapping wings.
- Rotational circulation: The rotational motion of insect wings (pronation and supination) induce additional circulation around the wing, leading to large lift force (Dickinson et al. 1999).
- Wake capture: Insects interact favorably with the wake vortices that are shed in the earlier cycles of flapping and this leads to additional aerodynamic forces (Dickinson et al. 1999; Birch et al. 2004).

The aforementioned unsteady aerodynamic mechanisms are responsible for the observed high performance of flapping insect wings at low Reynolds numbers.

13.1.2 Tandem Wing Aerodynamics

In contrast to the aerodynamics of single-winged insects, flow structures involved in tandem winged fliers are more complex. Dragonflies, nature's most ubiquitous, agile, and highly maneuverable fliers have tandem wings (a forewing and a hindwing). They generally flap their wings in a stroke plane that is 60° relative to the horizontal (Norberg 1975). High maneuverability of dragonflies is due to the presence of fore and hindwings that move independently of each other (Alexander 1984).

Multiple wings cause wing–vortex and wing–wing interactions resulting in complex lift and drag variations. Lan and Sun (2001) studied the elliptical airfoils flapping in tandem at phase differences $\psi = 0°, 90°$, and $180°$ by solving 2D incompressible Navier–Stokes (N-S) equations on moving over-set grids. They reported that in-phase stroking ($\psi = 0°$) produces the maximum lift and $\psi = 90°$ phase difference produces the minimum lift. Furthermore, computational fluid dynamics (CFD) simulations of Wang and Sun (2005) show that the forewing–hindwing interaction results in reduced lift forces. In addition, the simulations of Wang and Russell (2007) show that a dragonfly uses out-of-phase flapping to minimize the power consumption during hovering; and in-phase flapping during take-offs which require maximum power. With the experiments on robotic wings, Usherwood et al. (2008) showed that dragonflies employ wing phasing to remove swirl and improve the efficiency. In general, the vortex wake contains swirl which reduces the aerodynamic efficiency of the wings and the forewing–hindwing interaction can be either beneficial or detrimental to the performance of the wings.

13.1.3 Ground Effect

Apart from the wing–wing and wing–vortex interactions, the presence of a wall can influence the vortical structures and the vortex-induced forces. Gao and Lu (2008) studied a model wing flapping in a horizontal stroke plane near the ground and reported three force regimes, viz. force enhancement, force reduction, and force recovery regimes with the conclusion that both shed and rebound vortices decide the variation of the lift and drag forces. Liu et al. (2009) extended the study for clap and fling kinematics, and De Rosis (2015) for symmetric wings flapping in tandem. By high-resolution digital particle image velocimetry (DPIV), van Truong et al. (2013) studied the vortical structures surrounding a beetle's wing during take-off and showed that the ground enhances the size and shape of the LEV. Recently, Kolomenskiy et al. (2016) with 3D CFD simulations using an immersed interface method studied the take-off of an insect. Interestingly, whether the ground effect increases or decreases the aerodynamic forces is dictated by the kinematics of flapping motion and further investigations are necessary to improve our understanding of the ground–vortex interactions.

13.1.4 Suitability of IBM to Study Insect Flight

The current state-of-the-art insect flight research involves two steps: (1) accurate measurement of insect wing kinematics and flow field using high-speed imaging (Ennos 1989; Altshuler et al. 2005; Fry et al. 2005) and (2) replication of these kinematics either in mechanical fliers or in a CFD simulation. While experiments give a reliable estimate of forces, they provide only a limited information of the flow and obtaining

the complete flow field information over the rapidly oscillating insect wings in a fully non-intrusive manner is extremely challenging.

Numerical studies of insect flight necessitate the simulation of flow over rapidly oscillating wings. Conventional CFD methods require the generation of high-quality body-fitted structured or unstructured grid over the immersed boundaries, which is a daunting task in itself while dealing with flow past complex geometries. A poor quality grid can negatively impact the accuracy, stability, and convergence properties of the solver. Often, over complex geometries, the task of grid generation is carried out by dividing the computational domain into various sub-domains and generating the grid separately in these domains. Besides increasing the complexity of the solution algorithm, the deterioration in grid smoothness at the interface of the sub-domains can affect the stability of the solver. When the finite difference method is employed on a structured grid, the transformation of governing equations from the physical domain into the computational domain increases the per-grid-point operation count (Mittal and Iaccarino 2005).

While simulating the moving boundary problems with the help of a body-fitted grid, one encounters two difficulties:

- Transient re-meshing strategies are compulsory to accommodate the change in the shape or orientation of the body in fluid flow.
- A stable algorithm is necessary to project the old solution onto the new grid.

In addition to increasing the computational cost, these steps restrict the maximum time-step size that can be used for stable computations. IBM (Mittal and Iaccarino 2005) can be used to circumvent the aforementioned problems. IBM was first proposed by Peskin (1972) to study the flow around heart valves; numerous modifications have been proposed to the method since then (Goldstein et al. 1993; Fadlun et al. 2000; Kim and Choi 2006). In the past, IBM has been successfully used to simulate flows with complex moving boundaries such as flapping wings (Gilmanov and Sotiropoulos 2005; De Rosis 2014; Sudhakar and Vengadesan 2010a; Srinidhi and Vengadesan 2017a, b). IBM is particularly suited for flapping wing simulations due to the ease with which the kinematics can be imposed on the wings, high accuracy, and the computational advantage it provides. There are many variants of continuous forcing IBM available in the literature, and we make use of the immersed boundary projection method (IBPM) proposed by Taira and Colonius (2007).

In Sect. 13.2, the governing equations, the methodology of IBM solver, and a brief note on the multi-processor implementation of the IBM solver are detailed. In the subsequent sections, the IBM will be used to study the mechanism of vertical force generation in inclined stroke plane kinematics of insect flight, the effect of wing interference in the case of tandem wings, and the effect of ground on vortex dynamics of the flapping flight.

13.2 Governing Equations and the Numerical Method

We use the IBPM proposed by Taira and Colonius (2007) to develop a parallelized IBM solver. IBPM considers boundary force as a Lagrange multiplier to satisfy the no-slip condition; this is similar to the pressure acting as a Lagrange multiplier to satisfy the divergence-free constraint. Poisson equation for the pressure is modified to incorporate both divergence-free constraint as well as the no-slip constraint on the body. In IBM, the N-S equations are solved on a non-body conforming grid called Eulerian grid, $\mathscr{D}$, and a set of discrete Lagrangian points, ξ_k, represent the surface of a body, $\mathscr{B}$. Similar to most IBM, the incompressible flow is initially solved on an Eulerian grid, and the intermediate velocities are interpolated onto the Lagrangian points using an interpolation operator. The interpolated velocities are used to calculate the forces at the Lagrangian points and the forces are redistributed (regularized) to the nearby Eulerian grid points. In IBM, the Lagrangian points do not necessarily coincide with the underlying Eulerian grid. Hence, to interpolate the quantities to the Lagrangian points, discrete delta functions are used to exchange information between the Eulerian grid and the Lagrangian points.

The governing equations used are:

$$\frac{\partial \mathbf{u}}{\partial t} + \mathbf{u} \cdot \nabla \mathbf{u} = -\nabla p + \nu \Delta \mathbf{u} + \int_S \mathbf{f}(\boldsymbol{\xi}(s,t))\delta(\boldsymbol{\xi} - \mathbf{x})\mathrm{d}s, \tag{13.1}$$

$$\nabla \cdot \mathbf{u} = 0, \tag{13.2}$$

$$\mathbf{u}(\boldsymbol{\xi}(s,t)) = \int_S \mathbf{u}(\mathbf{x})\delta(\mathbf{x} - \boldsymbol{\xi})d\mathbf{x} = \mathbf{u}_B(\boldsymbol{\xi}(s,t)), \tag{13.3}$$

where $\mathbf{x} \in \mathscr{D}$, $\boldsymbol{\xi}(s,t) \in \mathscr{B}$, $\mathbf{u}$ represent the velocity vector, p is the pressure, ν is the kinematic viscosity, ∇ is the gradient operator, Δ is the Laplacian operator, and $\mathbf{f}$ represents the immersed boundary force. The boundary $\mathscr{B}$ is parameterized by s and moves at the velocity, $\mathbf{u}_B(\boldsymbol{\xi}(s,t))$. The governing equations are solved on staggered grids with pressure at the center of the cell and velocities located on the cell faces. The viscous terms are discretized with implicit Crank-Nicholson scheme and the second-order Adams-Bashforth scheme is used to discretize the nonlinear advective terms. The schemes yield a formal second-order accuracy in space and first-order accuracy in time.

The discretized governing equations can be written as:

$$\begin{pmatrix} A & G & -H \\ D & 0 & 0 \\ E & 0 & 0 \end{pmatrix} \begin{pmatrix} u^{n+1} \\ \phi \\ f \end{pmatrix} = \begin{pmatrix} r^n \\ 0 \\ u_B^{n+1} \end{pmatrix} + \begin{pmatrix} bc_1 \\ -bc_2 \\ 0 \end{pmatrix}, \tag{13.4}$$

where Hf corresponds to the last term in Eq.(13.1) which is the regularization operation. ϕ represents the pressure. The interpolation operator E is used to enforce the no-slip condition [Eq. (13.2)]; where, $Eu^{n+1} = u_B^{n+1}$. A, D, and G represent the implicit operator for velocity, discrete divergence, and gradient. r^n, bc_1, and bc_2 are

the explicit terms in the momentum equation, inhomogeneous terms resulting from the boundary condition of Laplacian operator and from the divergence operator, respectively. H and E represent the regularization and interpolation operators used to exchange information between the Eulerian and Lagrangian grid points. The operators are constructed using discrete delta function proposed by Roma et al. (1999). The present delta function is supported over three cells and has the form:

$$d(r) = \begin{cases} \frac{1}{6\Delta r}\left[5 - 3\frac{|r|}{\Delta r} - \sqrt{-3\left(1 - \frac{|r|}{\Delta r}\right)^2 + 1}\right] & \text{for} \quad 0.5\Delta r \le |r| \le 1.5\Delta r, \\ \frac{1}{3\Delta r}\left[1 + \sqrt{-3\left(\frac{r}{\Delta r}\right)^2 + 1}\right] & \text{for} \quad |r| \le 0.5\Delta r, \\ 0 & \text{otherwise}, \end{cases} \tag{13.5}$$

where Δr is the cell width. The delta function can only be used in uniform grids, so the extent of the domain in which the bodies move is discretized uniformly, stretched grids are used in the rest of the domain (Fig. 13.1).

Convolution of Eulerian background velocities with the delta function gives the velocities at the Lagrangian points,

$$\mathbf{u}(\boldsymbol{\xi}) = \int_x \mathbf{u}(\mathbf{x})\delta(\mathbf{x} - \boldsymbol{\xi})\mathbf{dx}, \tag{13.6}$$

the convolution yields:

$$u_k = \Delta x \Delta y \sum_i u_i d(x_i - \xi_k) d(y_i - \eta_k), \tag{13.7}$$

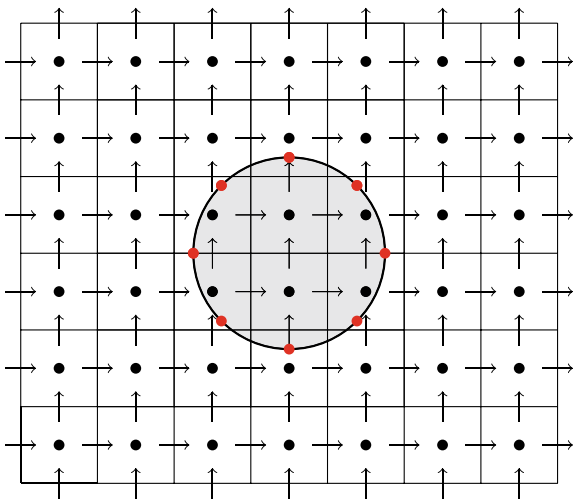

Fig. 13.1 Body $\mathscr{B}$, is represented by the shaded object immersed in a 2D domain $\mathscr{D}$ discretized by a staggered grid. Horizontal and vertical arrows ($\rightarrow$, $\uparrow$) denote the u and v velocity nodes, respectively. Pressure is located at the center of each cell depicted by circles ($\bullet$). Lagrangian points, $\boldsymbol{\xi}_k = (\xi_k, \eta_k)$, are shown by red circles

If $\gamma = \Delta x \Delta y$, Eq. (13.7) can be simplified as,

$$E_{k,i} = \gamma d(x_i - \xi_k) d(y_i - \eta_k), \tag{13.8}$$

The regularization operator H is also obtained by the convolution of Lagrangian values with the delta function, and it is equal to $-E^T$. We can formulate G and D such that $D = -G^T$.

$$\begin{pmatrix} A & G & E^T \\ G^T & 0 & 0 \\ E & 0 & 0 \end{pmatrix} \begin{pmatrix} u^{n+1} \\ \phi \\ f \end{pmatrix} = \begin{pmatrix} r^n \\ 0 \\ u_B^{n+1} \end{pmatrix} + \begin{pmatrix} bc_1 \\ -bc_2 \\ 0 \end{pmatrix}, \tag{13.9}$$

Considering both ϕ and f as Lagrange multipliers, we get:

$$Q \equiv [G, E^T], \quad \lambda \equiv \begin{pmatrix} \phi \\ f \end{pmatrix}, \quad r_1 \equiv r^n + bc_1, \quad r_2 \equiv \begin{pmatrix} -bc_2 \\ u_B^{n+1} \end{pmatrix}. \tag{13.10}$$

Using Eqs. (13.10), (13.9) can be simplified as below:

$$\begin{pmatrix} A & Q \\ Q^T & 0 \end{pmatrix} \begin{pmatrix} q^{n+1} \\ \lambda \end{pmatrix} = \begin{pmatrix} r_1 \\ r_2 \end{pmatrix}, \tag{13.11}$$

where scaling factors have been used to convert velocities, u^{n+1}, to fluxes, q^{n+1}, at cell faces. Thus, the steps in immersed boundary projection method are:

$$Aq^* = r_1 \qquad \text{(Solve for intermediate velocity)}, \tag{13.12}$$

$$Q^T B^N Q\lambda = Q^T q^* - r_2 \qquad \text{(Solve the modified Poisson equation)}, \tag{13.13}$$

$$q^{n+1} = q^* - B^N Q\lambda \qquad \text{(Projection step)}, \tag{13.14}$$

where B^N is an approximation of A^{-1}. Additional details about the algorithm and its implementation can be found in Taira and Colonius (2007). Major difference and advantage of IBPM are that it calculates the body forces and pressure values in a single step by solving Eq. (13.13).

Our code is based on the open-source code PetIBM developed by Krishnan (2015). We modified the code and added the capability to perform simulations with moving bodies. The C++ based code is parallelized using the open-source parallel programming library PETSc (Balay et al. 2019). Basic parallelization strategies and the necessary details of the implementation are given in Krishnan (2015). Here, we focus on the implementation details of the moving boundary simulations. In vector r_2 of Eq. (13.10), $u_B^{n+1} = 0$ for the flow over stationary bodies, and $u_B^{n+1} \neq 0$ for the flow over moving boundaries. We created a parallel array to distribute Lagrangian points to different processors. In simulations involving moving boundaries, the elements in the modified Poisson matrix $Q^T B^N Q$ changes due to the change in the position of Lagrangian points. This necessitates the modification of the matrix at the end of every time step. The matrix $Q^T B^N Q$ and the parallel distribution vector corresponding to the immersed boundary are destroyed and recreated after every time step. As the

creation of a parallelized matrix in PETSc is time consuming; the aforementioned step is the major bottleneck in the present implementation. Modification of Poisson matrix in IBPM increases the condition number of the matrix system. To solve the ill-conditioned system, we use Krylov sub-space iterative solvers with multigrid preconditioner.

13.3 The Mechanism of Force Generation in Flapping Flight

Of the three unsteady aerodynamic mechanisms presented in Sect. 13.1, delayed stall, i.e., enhanced force generation due to the attached LEVs is the most significant lift generation mechanism for insect flight. For a fruit-fly, which uses horizontal wing motion, the delayed stall generates enough force to support more than 85% of its total weight (Wu and Sun 2004). However, the functional significance of delayed stall in hovering insects which oscillate their wings along an inclined stroke plane is still less evident. While horizontal stroke plane motions rely on lift, drag on the wings in inclined stroke plane motions makes a significant contribution to support the weight (Wang 2004). Given the different strategies of weight support inherent in these horizontal plane and inclined plane wing motions, it is natural to expect that aerodynamic force generation mechanism in lift-dependent horizontal stroke plane wing motions is different than in drag-dependent inclined stroke plane wing motions.

In this work, we consider the following idealized wing kinematics for the flapping motion of insect wings which is schematically shown in Fig. 13.5.

Translational velocity,

$$\mathrm{v}(\tau) = -\sin\left(2\frac{c}{A_0}\tau\right), \tag{13.15}$$

Angular velocity confined to stroke reversal,

$$\omega(\tau) = \bar{\omega}\left[1 - \cos\left(\frac{2\pi(\tau - \tau_r)}{\Delta\tau_r}\right)\right]; \quad \tau_r \le \tau \le (\tau + \Delta\tau_r), \tag{13.16}$$

where τ is the non-dimensional time, c is the chord length of the wing, A_0 is the stroke amplitude, τ_r is the time at which the rotation starts, $\Delta\tau_r$ is the time required to perform the rotation, $\bar{\omega} = \frac{\Delta\theta}{\Delta\tau}$ is the average rotational speed, and $\Delta\theta$ is the change in AoA achieved in wing rotation.

Non-dimensional period of wing beat cycle (τ_c) can be found by the following relation,

$$2\frac{c}{A_0}\tau_c = 2\pi. \tag{13.17}$$

A flat plate of 2% thickness to chord ratio is used to model the wing cross section. The plate is discretized with 102 Lagrangian points ($\Delta s = 0.02$). The size of the rectangular computational domain chosen is ($-30c \le x \le 30c$, $-30c \le y \le 30c$).

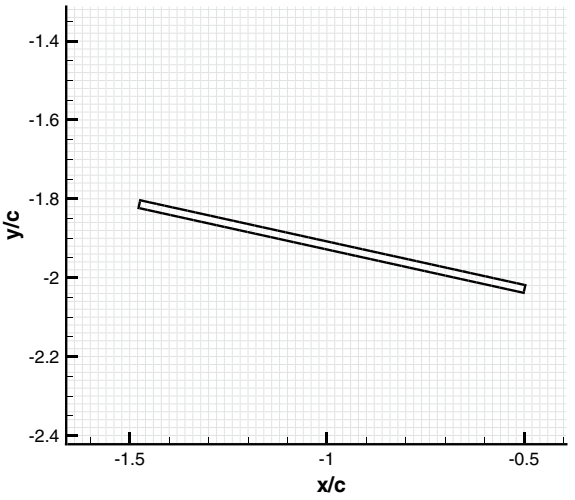

Fig. 13.2 Close up view of non-body conformal grid around the wing

A small area within the computational domain is discretized with uniform grid of $\Delta x = \Delta y = 0.02$. The size of this area is chosen in such a way that the wing is immersed within the uniform grid region throughout the stroke. The final size of the Eulerian grid in x- and y-direction for 2.5 chord lengths travel is 397 and 438, respectively. A picture of the wing immersed in the non-body conformal Cartesian grid is shown in Fig. 13.2. Every flapping cycle is discretized with 2000 time steps ($\Delta\tau_r = \tau_c/2000$). All the results presented in the subsequent sections are for the wing during its tenth cycle of flapping, by which time the forces and the flow reach a periodic state. The instantaneous forces are non-dimensionalized with $0.5\rho \mathrm{v}_{\mathrm{rms}}^2 c$. It has been confirmed that the results presented here are grid- as well as time-step independent.

We simulate the flapping wing with the following typical kinematic parameters: Reynolds number, $\mathrm{Re}(= \mathrm{v}_{\mathrm{max}} c/\nu) = 150$ where ν is the kinematic viscosity, stroke amplitude, $A_0 = 2.5c$, rotational period is 20% of the period of wing beat cycle ($\Delta\tau_r = 0.2\tau_c$), and stroke plane angle, $\beta = 62.8°$. The AoA during downstroke and upstroke are 50.6° and 15°, respectively. All these details are for the dragonfly hovering, similar to the simulations of Wang (2004), except that in our study a flat plate is used to model the cross section of the wing and the wing rotation in our study is confined to stroke reversal.

The time history of vertical force coefficient $\mathrm{C_V} = \frac{\mathrm{F_V}}{\frac{1}{2}\rho \mathrm{v_{rms}}^2 c}$ and horizontal force coefficient $\mathrm{C_H} = \frac{\mathrm{F_H}}{\frac{1}{2}\rho \mathrm{v_{rms}}^2 c}$ for one complete stroke is shown in Fig. 13.3; here, $\mathrm{F_V}$ and $\mathrm{F_V}$ are the vertical and horizontal forces on the wing, respectively. The stroke averaged horizontal force coefficient, $\overline{\mathrm{C_H}}$ is almost zero, which confirms that the simulation is for hovering motion. Since $\overline{\mathrm{C_H}}$ is almost zero in other simulations also, only the time history of $\mathrm{C_V}$ is presented in the subsequent sections. As has been

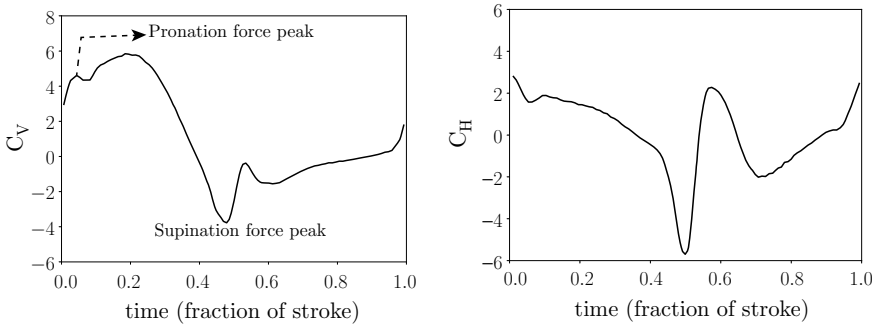

(a) Vertical force coefficient (b) Horizontal force coefficient

Fig. 13.3 Time history of force coefficients at Re = 150. The time between 0–0.5 is downstroke and 0.5–1 is upstroke

explained, downstroke induces positive C_V, and in upstroke negative C_V is generated over the flapping wing. The figure also shows the force peaks during the wing rotation (pronation and supination).

In the downstroke, two attached vortices are formed on either side of the wing as shown in Fig. 13.4a. The flow field is analogous to the flow past a bluff body in a laminar steady-state regime. The pressure drag formed over the wing is very high, so that the vertical force production is also high. The net aerodynamic force produced during the downstroke is almost perpendicular to the wing (Fig. 13.4a), implying the dominance of pressure forces over viscous forces. During upstroke, attached shear layers are formed over the wings without vorticity roll-up. The aerodynamic force is not perpendicular to the wing, but is more inclined to the wing surface (Fig. 13.4b), implying that viscous forces are also important in upstroke. It is clear from Fig. 13.4 that the upward component of aerodynamic force produced during the downstroke is much higher than the downward component of aerodynamic force generated during the upstroke.

The above analysis reveals a remarkable feature of the inclined stroke plane kinematics: insects utilize their tiny wing as a bluff body during downstroke, producing enormous pressure drag and as a streamlined body during upstroke, producing low skin-friction drag and this difference in drag helps insects to hover. Additional analyses (not discussed here) have confirmed that the delayed stall, which is the most important aerodynamic mechanism in horizontal stroke plane motions has marginal significance in inclined stroke plane kinematics (Sudhakar and Vengadesan, 2010b).

13.4 Wing Interference Effects

We discussed the mechanism of vertical force generation considering a single flapping wing in the previous section. Insects like dragonflies have two wings in tandem. To study the effect of wing interference, we consider tandem wings hovering in a qui-

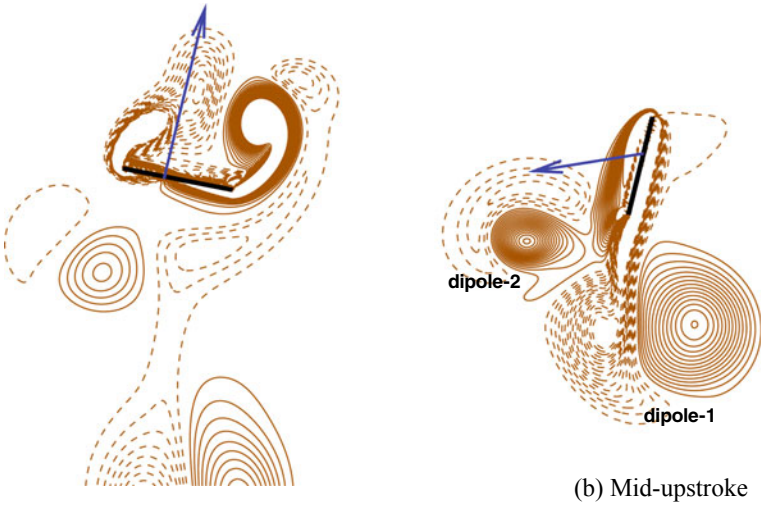

(a) Mid-downstroke

(b) Mid-upstroke

Fig. 13.4 Contours of vorticity and the instantaneous force acting on the wing during the middle of the half-strokes for Re = 150

escent fluid. The study demonstrates the feasibility of IBM in the study flows involving multiple moving bodies. The computational domain, boundary conditions, and the kinematics used in the study are shown in Fig. 13.5. We have used the following kinematics proposed by Wang (Wang, 2004):

$$[\mathrm{x}(t), \mathrm{y}(t)] = \frac{A_0}{2c}\cos(2\pi ft + \psi)(\cos\beta \sin\beta), \tag{13.18}$$

$$\alpha(t) = \alpha_0 - \alpha_m \sin(2\pi ft + \phi + \psi), \tag{13.19}$$

$$\mathrm{C_H} = \frac{\mathrm{F_H}}{\frac{1}{2}\rho \mathrm{U}^2 c}, \qquad \mathrm{C_V} = \frac{\mathrm{F_V}}{\frac{1}{2}\rho \mathrm{U}^2 c}, \tag{13.20}$$

where $[\mathrm{x}(t), \mathrm{y}(t)]$ is the position of the center of chord of the wing, $\alpha(t)$ is the angle made by the chord with the stroke plane, β is the stroke plane angle, ϕ is the phase difference between translation and rotation, f is the frequency of flapping, and A_0/c and α_m are the amplitudes of translation and rotation, respectively.

Velocity scale, $\mathrm{U} = \pi(A_0/c)f$, is related to oscillating translation. Reynolds number, $\mathrm{Re} = \mathrm{U}c/\nu = \pi f A_0 c/\nu$, is based on the maximum velocity of translation and the chord length. $T = 1/f$ is the time period of flapping. $\mathrm{C_H}$ and $\mathrm{C_V}$ represent the horizontal and vertical force coefficients respectively and ψ is the phase difference between flapping of forewing and hindwing. The size of the computational domain is $20c \times 20c$. The wing is immersed in a uniform grid of size $\Delta\mathrm{x}, \Delta\mathrm{y} = 0.01c$ and stretched everywhere else. The corresponding grid size is 992×992. We employ vorticity contours and backward finite-time Lyapunov exponent (FTLE) ridges to explain the time-varying forces resulting from the vortex dynamics.

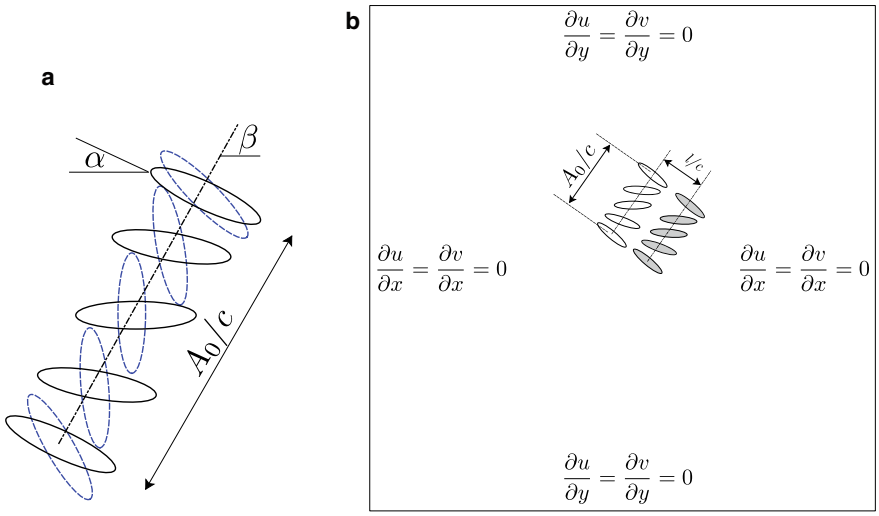

Fig. 13.5 **a** Positions of the elliptical foil in a flapping cycle is shown here. Solid lines represent the positions in downstroke and dashed lines represent the positions during upstroke. $\beta = \pi/3$ is the stroke plane angle, $A_0/c = 2.5$ stroke length, $\alpha_0 = \alpha_m = \pi/4$ is the maximum angle of attack, and Re $= 100$ in the study. **b** Boundary conditions and the computational domain used in the study are given here. Forewing and hindwing are represented by white and gray foils, respectively. The perpendicular distance between the stroke planes of the two wings is represented by l/c

The visualization of hovering flapping wings are presented in the following section to emphasize the importance of Lagrangian coherent structures (LCS) in the study of unsteady vortex dynamics. Further information about the calculation of backward FTLE can be found in Srinidhi and Vengadesan (2017b). The Reynolds number Re is 100 and the ratio of minor axis to major axis of the ellipse is 0.25. LCS in Fig. 13.7 show the attracting dynamic structures in the flow which entrain the surrounding fluid. Time-dependent behavior of individual vortices like stretching and merging can be kept track of LCS.

13.4.1 Force Variation and Vortical Structures in Tandem Wing Hovering

To study the effect of wing interference, the inter-wing distance and phase difference are varied. Inter-wing distances of $l = 1.1c$, $1.2c$, $1.3c$, $1.5c$, $1.7c$, $1.9c$ $2.1c$ and phase differences $\psi = 0°$ and $180°$ were considered in the study. The variation of C_V reaches a periodic state in 4–5 flapping cycles and the forces are averaged over a flapping cycle after the tenth cycle. The time-averaged vertical and horizontal force coefficients are denoted by $\overline{C}_V$ and $\overline{C}_H$, respectively. In hovering, the weight of the insect is supported by the vertical force and as such we focus further discussions

only on the variation of C_V. In this section, the variation of time-averaged force with inter-wing distance, the effect of wing kinematics on the force variation in a flapping cycle and the effect of phase difference between the forewing and the hindwings are presented.

13.4.1.1 In-Phase Stroking, $\psi = 0°$

Figure 13.6 shows that $\overline{C}_V$ of the forewing is larger in magnitude than the $\overline{C}_V$ of a single wing. The presence of the forewing results in the decrease of the vertical force on the hindwing; whereas, the converse is true in the case of the forewing and the effects of the wing interference reduce as the inter-wing distance increases. The vertical force generated by the flapping wings depends on the unsteady vortex dynamics. The evolution of vorticity and the corresponding variation of C_V at $l = 1.1c$ for the same are shown in Figs. 13.7 and 13.8, respectively.

Hindwing constantly operates in the wake of the forewing; due to the effect of wake on the LEV generation, C_V of the hindwing is less compared to the forewing. In the downstroke, the presence of trailing edge vortex of the forewing (TEV_F, Fig. 13.7b) has a detrimental effect on the growth of the LEV of the hindwing. In the upstroke, the hindwing is nearly vertical and it constantly moves in the downwash created by the forewing. The downwash increases the drag on the surface of the hindwing, consequently, C_V of the hindwing is less than a single-wing flapping system.

Figures 13.8a, b show the time variation of C_V at different inter-wing distances. For the sake of comparison, C_V variation of single-wing flapping is also plotted (dashed line). From Fig. 13.6, it is clear that forewing generates more force than a single flapping wing system, this shows that the presence of the hindwing enhances the force generation of the forewing. In Fig. 13.8a, b, the initial peak in vertical force at $t/T \approx 0.05$ is due to the reaction force provided by the fluid due to acceleration

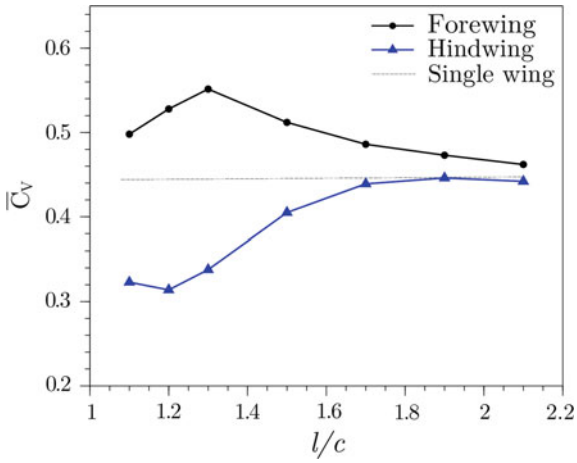

Fig. 13.6 $\overline{C}_V$ versus l/c of both fore and hindwing

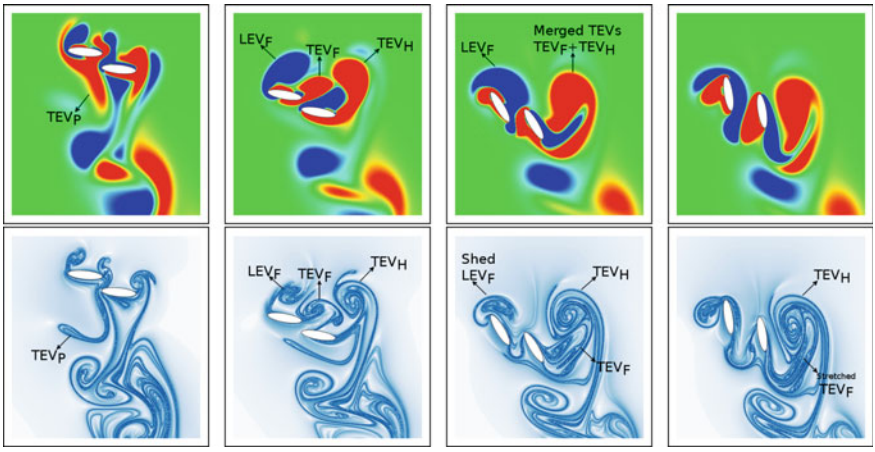

(a) $t/T = 0.1$ (b) $t/T = 0.3$ (c) $t/T = 0.5$ (d) $t/T = 0.7$

Fig. 13.7 Evolution of vorticity with time and LCS for $l = 1.1c$. Vorticity and LCS are plotted in alternating rows. Subscripts F and H represent fore and hindwings, respectively. Subscript P corresponds to the residual vorticity from the previous stroke or the shed vortex in the wake

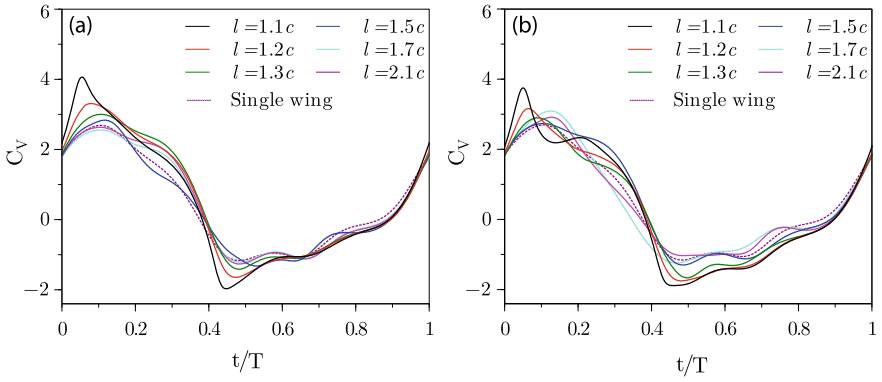

Fig. 13.8 **a** and **b** Time-varying C_V of forewing and hindwing, respectively

of the wings and rapid pitch-down rotation of the wings (Meng and Sun, 2016). Also, the counterclockwise (CCW) wake vortex represented by TEV_P (Fig. 13.8a, subscript P represents vorticity from the previous cycle) interacts with the wing and transfers momentum. This interaction, the so-called wake capture, also enhances the force. As the wings continue their downstroke, clockwise (CW) LEV is developed at the leading edge of the wings in accordance with the delayed stall mechanism (Fig. 13.7c). TEV_P is captured accurately in the LCS plot of Fig. 13.7a. At $t/T \approx 0.3$, TEV_P interacts with the hindwing, this corresponds to the local maxima in $\overline{C}_V$ of the hindwing (Fig. 13.8b). LEVs and TEVs of the forewing and the hindwing are represented by LEV_F, TEV_F and LEV_H, TEV_H, respectively. At $t/T \approx 0.5$, TEV

of the forewing is shed (TEV_F in Fig. 13.7c), and it interacts with the hindwing. As the wings start pitching up, due to the deceleration of the wings, $\overline{C}_V$ reaches its minimum value. The shed TEV of the forewing merges with the TEV of the hindwing ($TEV_F + TEV_H$ in Fig. 13.7d). The phenomenon of vortex merging is captured with finesse in the LCS contours. TEV_F gets sheared, stretched, and ultimately merges with TEV_H. As the wings continue with the upstroke, merged TEVs, and shed LEVs entrain surrounding fluid and transfer momentum. The jet created by the counter-rotating vortices forms a part of the total vertical force in the upstroke and the beginning of the downstroke.

Effect of inter-wing distance on force generation:

Figure 13.6 shows the effect of inter-wing distance on the cycle averaged vertical force. $\overline{C}_V$ of the hovering single wing is 0.446 (dashed line). Figure 13.9 presents the vorticity contours at various inter-wing distances. As the inter-wing distance increases, the effect of the forewing on the LEV generation of the hindwing decreases and $\overline{C}_V$ of the hindwing increases and reaches the $\overline{C}_V$ value of single flapping wing. When the wings are very close to each other, they act as a single system and the added mass effect which depends on the shape of the body and the acceleration of the fluid is prominent. As the separation between the wings increases, the added mass effect decreases and consequently the initial peak in C_V decreases (Fig. 13.8a, b). Figure 13.6 shows that $\overline{C}_V$ of fore and hindwings asymptotically reach $\overline{C}_V$ of the single-wing values at large enough inter-wing distances. In the downstroke of the wings, the maximum influence of the delayed stall mechanism on LEV generation occurs between $t/T = 0$ and 0.5. As the inter-wing distance increases, the effect of forewing downwash on the LEV generation of the hindwing decreases. Consequently, LEV of the hindwing grows in size and the vertical force generated by the hindwing increases. For $l < 1.3c$, the width of the wake increases as the l increases. For $l > 1.3c$, the width of the wake decreases as the inter-wing distance increases. Decrease in the width of the wake reduces the force generation. It is clear from Fig. 13.7 that LCS reveals structures which are otherwise hidden in vorticity plots.

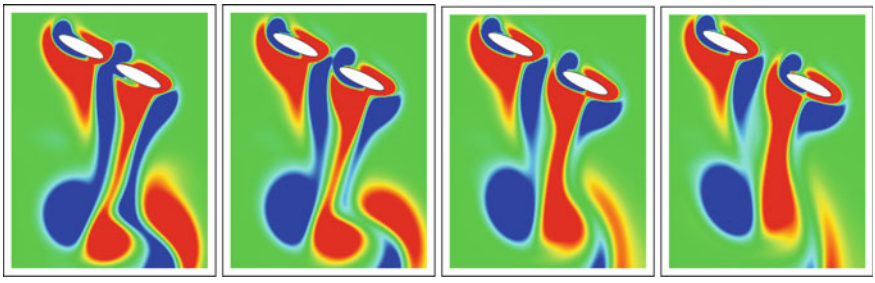

(a) $l = 1.3c$ (b) $l = 1.5c$ (c) $l = 1.7c$ (d) $l = 1.9c$

Fig. 13.9 Vorticity contours for different l at the end of the downstroke. As l increase size and strength of LEV and TEV increases

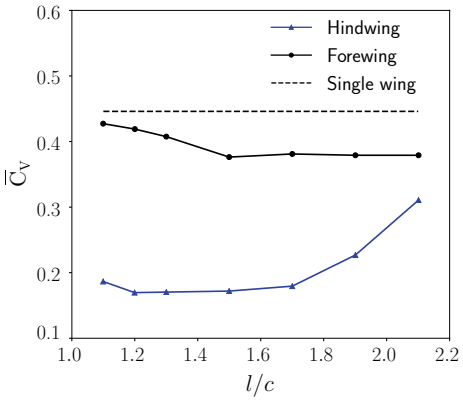

Fig. 13.10 $\overline{C}_V$ of both forewing and hindwing

13.4.1.2 Counter-Stroking, $\psi = 180°$

Figure 13.10 shows that the phase difference of $\psi = 180°$ reduces the variation of time-averaged vertical with the increasing inter-wing distance. Figures 13.11a, b represent the time variation of C_V for different l/c, for $\psi = 180°$. From Fig. 13.11a, it is clear that the presence of hindwing has a marginal effect on the C_V of the forewing. Hindwing in its downstroke generates lesser force compared to a single flapping wing, as it operates in a lower pressure area created by the shed TEV of the forewing. As the inter-wing distance increases, the effect of forewing on the force generation of hindwing decreases and consequently, for $l > 1.5c$ vertical force generation of the hindwing increases rapidly (Fig. 13.11b). Typical variation of C_V is explained for $l = 1.1c$. Figure 13.12 shows the evolution of vorticity and LCS contours over time.

Hindwing is at the beginning of its upstroke when the forewing is at the beginning of its downstroke (Fig. 13.12a). The initial peak in C_V is reduced because of the presence of the LEV of the hindwing (Fig. 13.11a). At $t/T = 0.3$, TEV of the forewing interacts with the CCW vorticity of the hindwing, creating a low-pressure region near the lower surface of the forewing (Fig. 13.12b). This corresponds to the minima in C_V of the forewing at $t/T \approx 0.3$. As the forewing moves away from the hindwing (Fig. 13.12c), the pressure on the lower surface of the wing increases and consequently C_V increases (Fig. 13.12c) and reaches a local maxima at $t/T = 0.3$. At $t/T = 0.3$, TEV of the forewing and CCW vorticity of the hindwing merge together and form a region of low pressure between the two wings (Fig. 13.12c). As the hindwing starts its downstroke, it interacts with the merged CCW vortex, this wake capture increases the vertical force generation of the hindwing. In Fig. 13.12c, it is clear that the C_V maxima at $t/T = 0.6$ is greater in magnitude than C_V of a single-wing flapping due to the interaction with the merged vortex (Fig. 13.12d).

After the wake capture, as the hindwing continues its downstroke, the downwash of the forewing and the LEV shed by the forewing result in a sudden fall in the vertical force. For the rest of its downstroke, the hindwing operates in a low-pressure

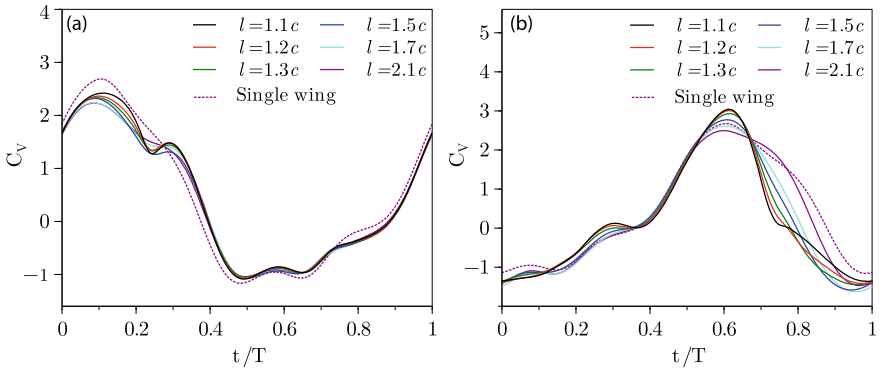

Fig. 13.11 **a** and **b** Time-varying C_V of forewing and hindwing, respectively

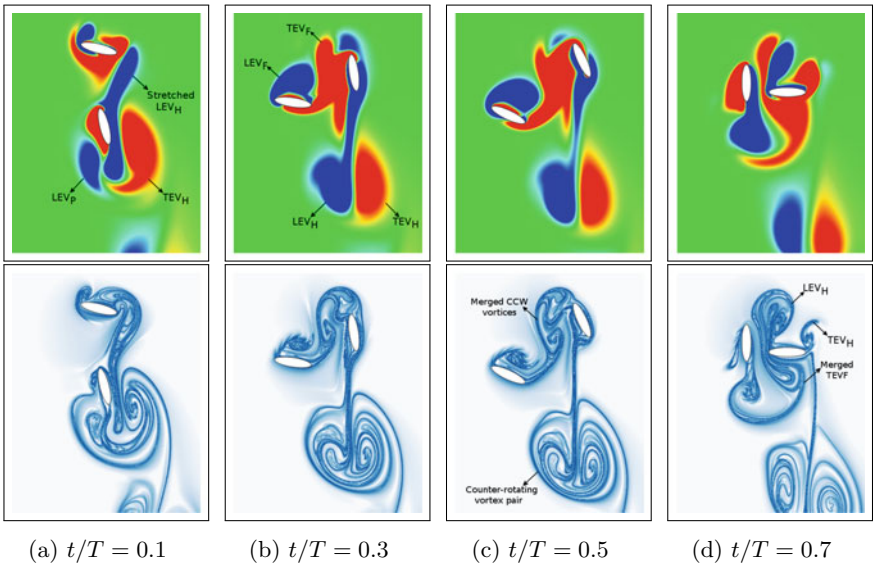

(a) $t/T = 0.1$ (b) $t/T = 0.3$ (c) $t/T = 0.5$ (d) $t/T = 0.7$

Fig. 13.12 Evolution of vorticity with time and LCS for $l = 1.1c$. Vorticity and LCS are plotted in alternating rows

region created by the shed LEV of the forewing, the merged vortex and the growing LEV. This results in the sudden drop in the vertical force generation of the hindwing for $t/T > 0.7$. In comparison with a single-wing flapping where the delayed stall mechanism generates much of the vertical force. Besides, a part of the shed LEV of the forewing and the CW shear layers merge with the LEV of the hindwing (Fig. 13.12d) and enhance the delayed stall effect. This results in a further reduction of pressure around the wing and is the major reason for the decreased vertical force generation of the hindwing. A pair of counter-rotating vortices are shed in every flapping cycle. The

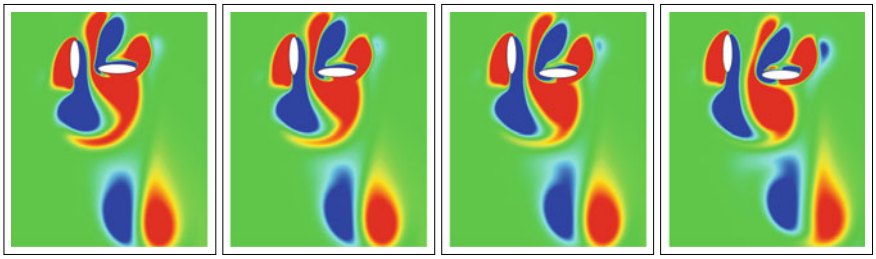

Fig. 13.13 Vorticity contours for different l at the end of the downstroke. As l increase size and strength of LEV and TEV increases

vortex pair has low swirl component. This wake with predominant vertical velocity increases the stability of the body in hovering.

Effect of inter-wing distance:

Figure 13.13 presents the vorticity contours at different inter-wing distances. $\overline{C}_V$ of the forewing slightly decreases initially, for $l < 1.5c$ and remains nearly constant at greater distances. The effect is apparent as the vortical structures of the forewing look similar. $\overline{C}_V$ of the hindwing increases slowly for $l < 1.5c$ and increases rapidly for $l > 1.5c$. For $l \geq 1.7c$, there is no formation of the merged vortex, this reduces the peak C_V of the hindwing at $t/T = 0.6$ (Fig. 13.11b) as the effect of wake capture is diminished. For $l > 1.5c$, due to the reduced wing–wing interactions, and decreased effect of merged vortex in reducing the pressure around the hindwing, the delayed stall mechanism becomes more effective in the force generation (Fig. 13.11b).

13.5 Effect of Ground on the Force Generation

In this section, we study the effect of ground on the vortex dynamics and the force production of a single flapping wing. The study is carried out in a domain of size: $-20c \leq x \leq 20c$, $-1c \leq y \leq 20c$ on a grid with uniform grid dimensions of $0.01c$. Figure 13.14 represents the details of the computational domain and boundary conditions used in the study.

Figure 13.15a represents the $\overline{C}_V$ versus the ground clearance D/c. Figure 13.15b shows the time-varying vertical force C_V versus the non-dimensionalized time plotted at different heights from the ground. For the sake of clarity, only C_V variations pertaining to $D/c = 0.5$, 1, 2, 3, 5, and without ground effect cases are plotted.

Similar to Gao and Lu (2008), the variation of $\overline{C}_V$ can be grouped into three regimes: force enhancement, force reduction, and force recovery regimes. For $D/c < 2$, as the wing moves closer to the ground, force generation increases, and the ground effect is dominant; the force behavior lies in the force enhancement regime. For $2 < D/c < 4$, $\overline{C}_V$ is lesser than the values for the case with $D/c = 0.5$ as well as

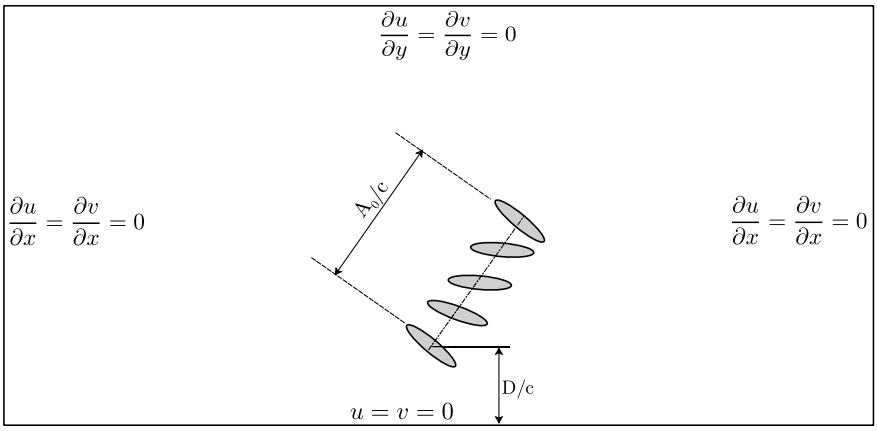

Fig. 13.14 Computational domain and the boundary conditions used in the study are represented here. The non-dimensional clearance from the ground D/c is the vertical distance between the center of the wing and the ground when the wing is at the end of its downstroke

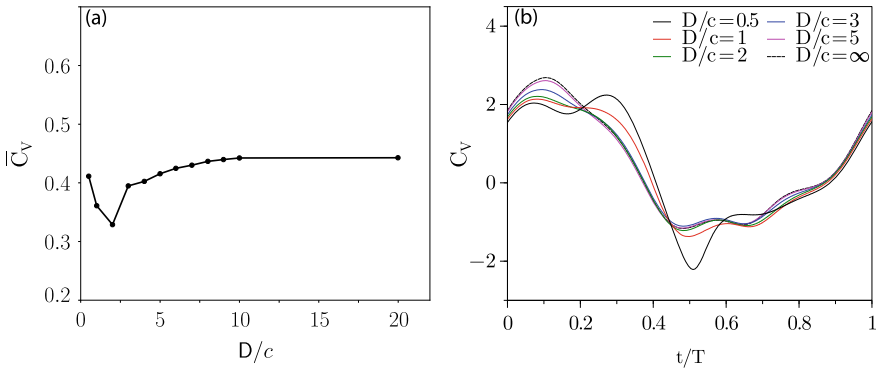

Fig. 13.15 **a** Time-averaged vertical force versus ground clearance. **b** Vertical force versus time

$\overline{C}_{V_\infty}$, and the force behavior changes from force enhancement to force recovery regime. This regime is called force reduction regime. In the force recovery regime ($D/c > 4$), the wing experiences increased vertical forces due to the reverse Kármán vortex shedding and $\overline{C}_V$ slowly reaches $\overline{C}_{V_\infty}$. Figure 13.16 shows the evolution of vortical structures with time, along with the corresponding pressure contours for $D/c = 0.5$. Velocity vectors are superimposed on vorticity plots to visualize the interaction between fluid and the ground.

In Fig. 13.15b, C_V initially increases and reaches its maximum at $t/T \approx 0.08$. This initial peak is due to the acceleration of the wing, and the rapid pitch-down rotation. After the initial peak, C_V slowly decreases and starts increasing at $t/T \approx 0.2$. In Fig. 13.16a, b, the vortex which is near the lower surface of the wing adds a CW circulation to the fluid displaced by the wing, this reduces the effect of the ground on

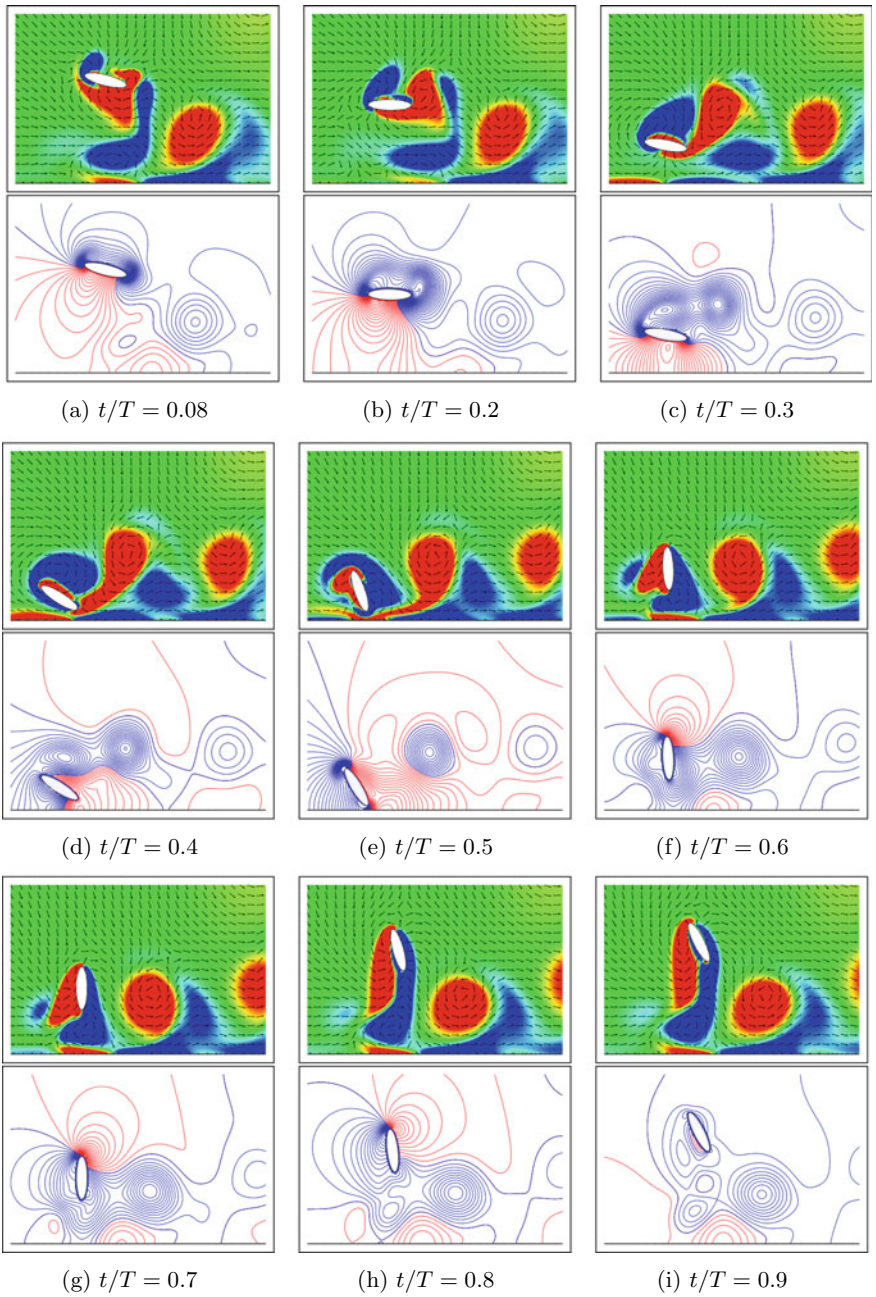

(a) $t/T = 0.08$ (b) $t/T = 0.2$ (c) $t/T = 0.3$

(d) $t/T = 0.4$ (e) $t/T = 0.5$ (f) $t/T = 0.6$

(g) $t/T = 0.7$ (h) $t/T = 0.8$ (i) $t/T = 0.9$

Fig. 13.16 Evolution of vorticity and pressure with time at $D/c = 0.5$. Velocity vectors are superimposed on vorticity. Vorticity and pressure are plotted in alternating rows. Red represents CCW vorticity and positive pressure, and blue represents CW vorticity and negative pressure. Contour levels for both vorticity and pressure are from -1 to 1

the generation of vertical force. As the wing continues its downstroke, the CW vortex advects downstream and away from the wings facilitating cushion effect; this results in the direct impingement of the fluid on the ground. The increasing pressure on the lower surface of the wing causes an increase in C_V. This effect is analogous to a jet impinging on a surface. Along with the cushion effect, the formation of leading-edge vortex (LEV) in accordance with the delayed stall mechanism creates a low-pressure region on the upper surface of the wing. A counterclockwise (CCW) trailing edge vortex (TEV) is also created at the trailing edge of the wing. LEV coupled with the cushion effect is the reason for the high $\overline{C}_V$ observed in the near ground cases. The flow generated by the wing creates shear layers on the ground. As the wing starts pitching up, LEV and TEV of the wing are shed (Fig. 13.16c) causing a total loss of lift. At $t/T \approx 0.5$, the wing interacts with the shear layer on the ground and disrupts it (Fig. 13.16e). Due to the severe gradients created, C_V becomes minimum. At $t/T \approx 0.5$, the wing starts its upstroke and the lift slowly starts increasing because of the induced velocity of the jet created by the shed LEV and the shed TEV. For most part of the upstroke, the wing is vertical and is surrounded by a low-pressure region (pressure plots of Fig. 13.16f–h), as a result, the lift generated in the upstroke is less compared to the downstroke.

Figure 13.17 shows the evolution of vortical structures at $D/c = 1$. Important flow features in the present case are the rebound vortices. LEV and TEV shed in the previous stroke strike the ground and rebound, and the shed LEV forms a low-pressure region below the lower surface of the wing (Fig. 13.17a). Between $t/T = 0.2$ and 0.4, the wing interacts with the CW rebound vortex, (Fig. 13.17b–d). The presence of the rebound vortex reduces the cushion effect on the wing, as a result, C_V decreases compared to $D/c = 0.5$. The LEV shed at the end of the downstroke strikes the ground and forms a new rebound vortex. An important observation we made is the change in the effective angle of attack (AoA) of the wing caused by the flow created by the CW rebound vortex. When the wing is in its downstroke, the circulation added by the rebound vortex to the surrounding fluid changes the AoA of the wing. Depending on the size and strength of the CW rebound vortex, the vertical force generated by the wing may either increase or decrease.

At $D/c = 2$, the induced velocity of the jet created by the rebound vortices generates most of the force. The prominent flow feature at this ground clearance is the presence of a sustained CW rebound vortex (Fig. 13.18a). LEV shed by the wing at the end of the downstroke feeds the rebound vortex from the previous stroke. Shed TEV of the wing gets stretched by the shear layer at the ground, loses its strength and eventually dissipates. As the ground clearance increases, the induced velocity of the jet created by the shed vortices dominates the force generation. The flow structures at the beginning of the downstroke for $D/c = 2$, 5, and out-of-ground effect cases are shown in Fig. 13.18. The figures show that the effect of ground is negligible for $D/c > 5.0$ as flow structures are almost similar (Fig. 13.18b, c).

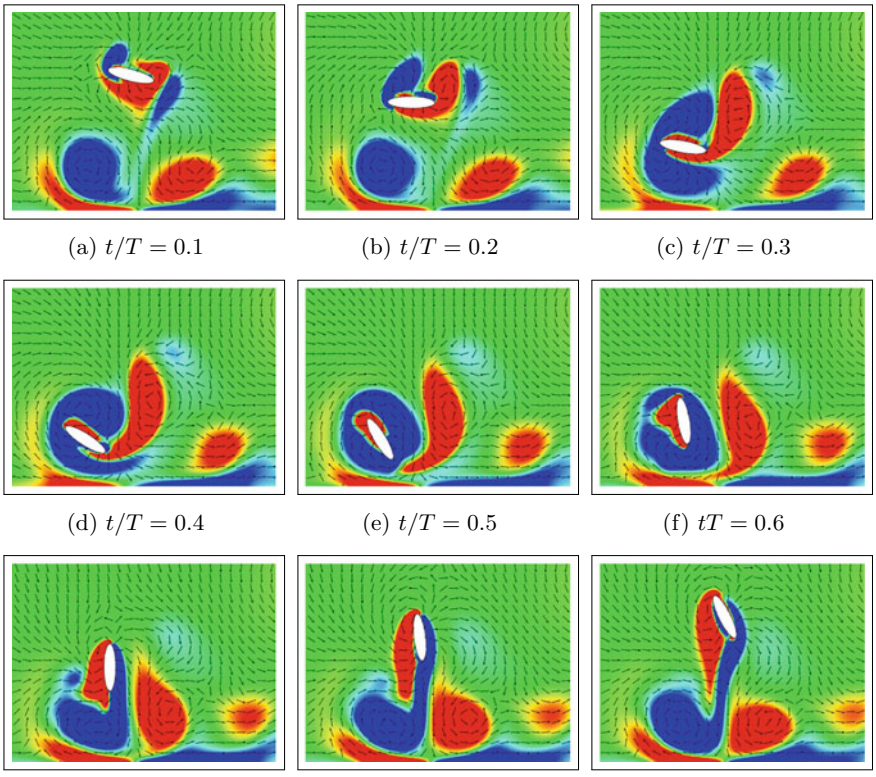

(a) $t/T = 0.1$ (b) $t/T = 0.2$ (c) $t/T = 0.3$

(d) $t/T = 0.4$ (e) $t/T = 0.5$ (f) $tT = 0.6$

(g) $t/T = 0.7$ (h) $t/T = 0.8$ (i) $t/T = 0.9$

Fig. 13.17 Evolution of vorticity with time for $D/c = 1$. Velocity vectors are superimposed on vorticity to visualize ground effect

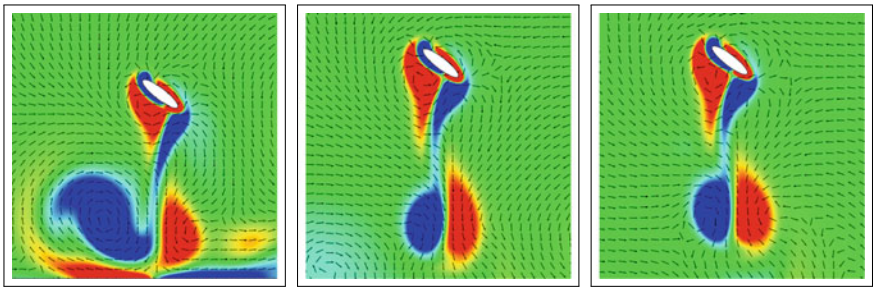

(a) $D/c = 2$ (b) $D/c = 5$ (c) $D/c = \infty$

Fig. 13.18 Vorticity contours at $t/T = 0.1$. Velocity vectors are superimposed on vorticity to visualize ground effect

13.5.1 A Note on Three-Dimensionality and Wing Flexibility

In this article, we have not considered two important effects relevant to insect flight: (1) finite aspect ratio of the wings and (2) wing flexibility. Various researchers have employed IBM, due to its versatility, to study the influence of these two and related parameters on the insect aerodynamics. These studies focused on the effect of the following parameters on the force production by flapping insect wings: three-dimensional wingtip vortices on finite aspect ratio wings (Moriche et al. 2016), effect of wing kinematic parameters (Han et al. 2018), complex maneuvering (Bode-Oke et al. 2018), wing flexibility (Shahzad et al. 2018), fluid–structure–acoustics interaction (Wang and Tian 2019), and complete wing-body models (Minami et al. 2014).

13.6 Conclusion

In this chapter, we presented the application of immersed boundary projection method to study the unsteady aerodynamics of insect flight. Following a brief review of the unsteady aerodynamic mechanisms involved in the insect flight, we presented the numerical implementation of the moving-body and multi-processor implementation of the present IBPM algorithm. The unsteady flow structures and aerodynamic forces acting on an idealized 2D dragonfly model wing were studied by numerically solving the N-S equations with the IBPM formulation. The chapter covered the kinematics and flow physics of the flapping flight with the focus on three major aspects of the flight: (1) the mechanism of vertical force generation, (2) the forewing–hindwing interaction in the case of tandem wings, and (3) the effect of ground on force generation. Spatio-temporal dynamics of vorticity field and Lagrangian coherent structures are used to understand the physics behind the force variation in inclined stroke plane kinematics. Our results suggest that the delayed stall mechanism is not the dominant lift generation mechanism in the case of such kinematics. Insects using inclined stroke kinematics use their wings as a bluff body in downstroke, and as a streamlined body during upstroke; this difference in operation helps in large vertical force generation. In the presence of tandem wings, in-phase stroking of the wings produces maximum vertical force and the out-of-phase stroking generates the least vertical force. Furthermore, the ground effect can be grouped into three regimes: force enhancement, force reduction, and force recovery regimes, depending on the non-dimensional ratio of distance between the ground to chord length.

It is worth emphasizing here that the immersed boundary method would be the ideal choice to simulate fluid flow over rapidly oscillating insect wings. Moreover, the study of interference effect and ground effect require handling multiple bodies coming very close to each other. IBM is instrumental in simulating flows around multiple bodies with complex kinematics. With conventional body-fitted methods,

it would be practically impossible to handle such situations without re-meshing operations and excessive human intervention. This situation is directly dealt with using immersed boundary methods, thus enabling us to easily study the physics in such scenarios.

References

Alexander DE (1984) Unusual phase relationships between the forewings and hindwings in flying dragonflies. J Exp Biol 109(1):379–383

Altshuler DL, Dickson WB, Vance JT, Roberts SP, Dickinson MH (2005) Short-amplitude high-frequency wing strokes determine the aerodynamics of honeybee flight. Proc Natl Acad Sci 102:18213–18218

Balay S, Abhyankar S, Adams MF, Brown J, Brune P, Buschelman K, Dalcin L, Dener A, Eijkhout V, Gropp WD, Kaushik D, Knepley MG, May DA, McInnes LC, Mills RT, Munson T, Rupp K, Sanan P, Smith BF, Zampini S, Zhang H, Zhang H (2019) PETSc web page

Birch JM, Dickson WB, Dickinson MH (2004) Force production and flow structure of the leading edge vortex on flapping wings at high and low Reynolds numbers. J Exp Biol 207(7):1063–1072

Bode-Oke AT, Zeyghami S, Dong H (2018) Flying in reverse: kinematics and aerodynamics of a dragonfly in backward free flight. J R Soc Interface 15(143):20180102

De Rosis A (2014) On the dynamics of a tandem of asynchronous flapping wings: lattice Boltzmann-immersed boundary simulations. Phys A Stat Mech Appl 410:276–286

De Rosis A (2015) Ground-induced lift enhancement in a tandem of symmetric flapping wings: lattice Boltzmann-immersed boundary simulations. Comput Struct 153:230–238

Dickinson MH, Lehmann FO, Sane SP (1999) Wing rotation and the aerodynamic basis of insect flight. Science 284(5422):1954–1960

Ellington CP (1984a) The aerodynamics of hovering insect flight. III. Kinematics. Philos Trans R Soc Lond B Biol Sci 305(1122):41–78

Ellington CP (1984b) The aerodynamics of hovering insect flight. VI. Lift and power requirements. Philos Trans R Soc Lond B Biol Sci 305(1122):145–181

Ellington CP, van den Berg C, Willmott AP, Thomas ALR (1996) Leading-edge vortices in insect flight. Nature 384(6610):626

Ennos R (1989) The kinematics and aerodynamics of the free flight of some Diptera. J Exp Biol 142:49–85

Fadlun EA, Verzicco R, Orlandi P, Mohd Yusof J (2000) Combined immersed-boundary finite-difference methods for three-dimensional complex flow simulations. J Comput Phys 161(1):35–60

Fry SN, Sayaman R, Dickinson MH (2005) The aerodynamics of hovering flight in Drosophila. J Exp Biol 208:2303–2318

Gao T, Lu XY (2008) Insect normal hovering flight in ground effect. Phys Fluids 20(8):087101

Gilmanov A, Sotiropoulos F (2005) A hybrid Cartesian/immersed boundary method for simulating flows with 3D, geometrically complex, moving bodies. J Comput Phys 207(2):457–492

Goldstein D, Handler R, Sirovich L (1993) Modeling a no-slip flow boundary with an external force field. J Comput Phys 105(2):354–366

Han J, Yuan Z, Chen G (2018) Effects of kinematic parameters on three-dimensional flapping wing at low Reynolds number. Phys Fluids 30(8):081901

Kim D, Choi H (2006) Immersed boundary method for flow around an arbitrarily moving body. J Comput Phys 212(2):662–680

Kolomenskiy D, Maeda M, Engels T, Liu H, Schneider K, Nave JC (2016) Aerodynamic ground effect in fruitfly sized insect takeoff. PLoS One 11(3):e0152072

Krishnan A (2015) Towards the study of flying snake aerodynamics, and an analysis of the direct forcing method. Ph.D. thesis
Lan SL, Sun M (2001) Aerodynamic properties of a wing performing unsteady rotational motions at low Reynolds number. Acta Mech 149(1–4):135–147
Liu Y, Liu N, Lu X (2009) Numerical study of two-winged insect hovering flight. Adv Appl Math Mech 1(4):481–509
Meng X, Sun M (2016) Wing kinematics, aerodynamic forces and vortex-wake structures in fruit-flies in forward flight. J Bionic Eng 13(3):478–490
Minami K, Suzuki K, Inamuro T (2014) Free flight simulations of a dragonfly-like flapping wing-body model using the immersed boundary-lattice Boltzmann method. Fluid Dyn Res 47(1):015505
Mittal R, Iaccarino G (2005) Immersed boundary methods. Annu Rev Fluid Mech 37:239–261
Moriche M, Flores O, García-Villalba M (2016) Three-dimensional instabilities in the wake of a flapping wing at low Reynolds number. Int J Heat Fluid Flow 62:44–55
Norberg RÅ (1975) Hovering flight of the dragonfly *Aeschna Juncea* L., kinematics and aerodynamics. In: Swimming and flying in nature. Springer, Boston, pp 763–781
Peskin CS (1972) Flow patterns around heart valves: a numerical method. J Comput Phys 10(2):252–271
Platzer MF, Jones KD, Young J, Lai JCS (2008) Flapping wing aerodynamics: progress and challenges. AIAA J 46(9):2136–2149
Roma AM, Peskin CS, Berger MJ (1999) An adaptive version of the immersed boundary method. J Comput Phys 153(2):509–534
Sane SP (2003) The aerodynamics of insect flight. J Exp Biol 206(23):4191–4208
Shahzad A, Tian F-B, Young J, Lai JCS (2018) Effects of Hawkmoth-like flexibility on the aerodynamic performance of flapping wings with different shapes and aspect ratios. Phys Fluids 30(9):091902
Shyy W, Aono H, Chimakurthi SK, Trizila P, Kang CK, Cesnik CES, Liu H (2010) Recent progress in flapping wing aerodynamics and aeroelasticity. Prog Aerosp Sci 46(7):284–327
Srinidhi NG, Vengadesan S (2017a) Ground effect on tandem flapping wings hovering. Comput Fluids 152:40–56
Srinidhi NG, Vengadesan S (2017b) Lagrangian coherent structures in tandem flapping wing hovering. J Bionic Eng 14(2):307–316
Sudhakar Y, Vengadesan S (2010a) Flight force production by flapping insect wings in inclined stroke plane kinematics. Comput Fluids 39(4):683–695
Sudhakar Y, Vengadesan S (2010b) The functional significance of delayed stall in insect flight. Numer Heat Transf Part A Appl 58:65–83
Taira K, Colonius T (2007) The immersed boundary method: a projection approach. J Comput Phys 225(2):2118–2137
Usherwood JR, Lehmann FO (2008) Phasing of dragonfly wings can improve aerodynamic efficiency by removing swirl. J R Soc Interface 5(28):1303–1307
van Truong T, Kim J, Kim MJ, Park HC, Yoon KJ, Byun D (2013) Flow structures around a flapping wing considering ground effect. Exp Fluids 54(7):1575
Wang ZJ (2004) The role of drag in insect hovering. J Exp Biol 207(23):4147–4155
Wang ZJ, Russell D (2007) Effect of forewing and hindwing interactions on aerodynamic forces and power in hovering dragonfly flight. Phys Rev Lett 99(14):148101
Wang JK, Sun M (2005) A computational study of the aerodynamics and forewing-hindwing interaction of a model dragonfly in forward flight. J Exp Biol 208(19):3785–3804
Wang L, Tian F-B (2019) Numerical study of flexible flapping wings with an immersed boundary method: fluid-structure-acoustics interaction. J Fluids Struct 90:396–409
Wu JH, Sun M (2004) Unsteady aerodynamic forces of a flapping wing. J Exp Biol 207:1137–1150